Probing the Role of Single Defects on the Thermodynamics of Electric-Field Induced Phase Transitions

S. V. Kalinin,[1,*] S. Jesse,[1] B. J. Rodriguez,[1] Y. H. Chu,[2] R. Ramesh,[2] E. A. Eliseev,[3] and A. N. Morozovska[3]
[1]*Oak Ridge National Laboratory, Oak Ridge, Tennessee 37831, USA*
[2]*Department of Physics and Department of Materials Science and Engineering, University of California, Berkeley, California 94720, USA*
[3]*National Academy of Science of Ukraine, Kiev, Ukraine*
(Received 18 July 2007; published 18 April 2008)

The kinetics and thermodynamics of first order transitions are universally controlled by defects that act as nucleation sites and pinning centers. Here we demonstrate that defect-domain interactions during polarization reversal processes in ferroelectric materials result in a pronounced fine structure in electromechanical hysteresis loops. Spatially resolved imaging of a single defect center in multiferroic $BiFeO_3$ thin film is achieved, and the defect size and built-in field are determined self-consistently from the single-point spectroscopic measurements and spatially resolved images. This methodology is universal and can be applied to other reversible bias-induced transitions including electrochemical reactions.

DOI: 10.1103/PhysRevLett.100.155703 PACS numbers: 64.60.Q−, 77.80.Dj, 85.50.Gk

Polarization switching in ferroelectric materials is the functional basis of applications including nonvolatile memories [1] and data storage [2]. These applications have stimulated extensive effort toward understanding the thermodynamic stability of the ferroelectric phase in constrained geometries and fundamental mechanisms for polarization reversal. Static domain structures and polarization distributions in low-dimensional systems and in the vicinity of bulk and interfacial defects have been extensively studied theoretically using Ginzburg-Landau [3] and first-principles theories [4]. A wealth of experimental information on polarization behavior at surfaces and in ultrathin films is becoming available with the emergence of grazing incidence x-ray methods [5] and electron microscopies [6].

The experimental and theoretical progress in understanding static polarization behavior is belied by the lack of knowledge on polarization dynamics. Landauer has demonstrated that the experimentally observed switching fields correspond to impossibly large ($\sim 10^3$–10^5 kT) values for the nucleation activation energy [7]. This discrepancy is resolved by postulating the presence of discrete switching centers initiating low-field nucleation. The spatial and energy distribution of the nucleation centers has become the central component of statistical theories for macroscopic polarization switching [8]. Notably, this behavior is universal to all first order phase transitions including solidification, martensitic phase transformations, and phenomena such as plastic deformation and electrochemical reactions, in which the formation of a new phase is always initiated at specific defect sites or is controlled by defect dynamics.

Recently, development of piezoresponse force microscopy (PFM) and focused x-ray imaging has allowed stroboscopic (PFM) [9,10] and real-time (x-ray) [11] measurements of domain growth in the uniform field of capacitor structures and visualization of nucleation sites. On free surfaces, localized switching by PFM has been used to directly measure domain wall geometry and growth rate, and thus, disorder in the system [12]. The mesoscopic observations of moving domain front geometry and kinetics allow direct comparison with well-known models for statistical physics of disordered systems [13,14]. The spatially resolved *imaging* studies are complemented by *spectroscopic* studies of the switching process, in which the measured electromechanical response as a function of dc tip bias provides information on the size of the domain formed below the tip [15]. The variation of nucleation biases along the surface has been used to map the random-field and random-bond components of the disorder potential, and establish the role of ferroelastic domain walls on switching [16]. However, whether the effect of a *single* localized defect on local polarization switching can be determined has yet to be resolved.

The observation of polarization switching on a single defect level requires (a) knowledge of the defect signature on local piezoresponse force spectroscopy (PFS) spectra, (b) sufficiently high sensitivity to detect a single defect, and (c) a model system with a defect larger than the characteristic spatial resolution. These conditions are similar to those in, e.g., single molecule optical microscopy, in which molecular size is well below spatial resolution, but detection of single molecules is possible due to large molecule-molecule separation. Here we predict the defect signature on local spectra, and demonstrate experimental observation of a single defect.

Simple estimates suggest that the characteristic defect size responsible for polarization switching in ferroelectrics is ~1–2 nm, well below PFM resolution (>10 nm). As a model system with low density of structural defects and high surface stability, we have chosen epitaxial (100) $BiFeO_3$ thin films [17]. Note the nearly ideal surface with roughness of 1.3 nm (after 1st order line subtraction) devoid of visible topographic defects, as shown in Fig. 1(a). The spatial variability of switching behavior is studied by switching spectroscopy PFM (SS-PFM) [18]. The majority of the sample surface exhibits nearly ideal hysteretic behavior (not shown). However, in several locations the recorded loops exhibit a pronounced fine structure. Several examples are shown in Fig. 1(d), in which single and multiple shoulders are evident. This behavior can be further illustrated in the first numerical derivative of the hysteresis loops, as shown in Figs. 1(e)–1(g). Notably, these fine-structure features are highly reproducible (up to 256 loops have been collected at a single point with negligible variation) and also change gradually between adjacent locations.

The observed loop fine structure suggests local deviations in the switching process from that in an ideal material due to defect-domain interactions. To determine the effect of a defect on polarization switching, we analyze the switching process within the framework of the Landauer-Molotskii model [7,19]. The free energy of the semiellipsoidal domain is

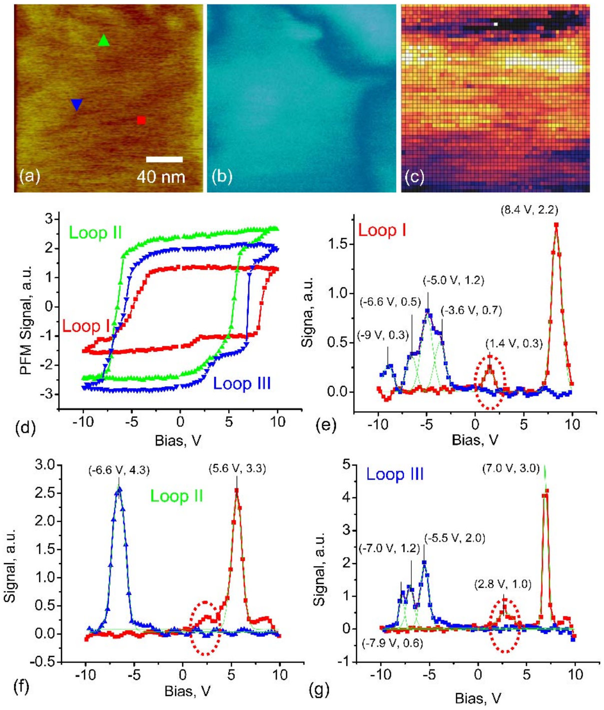

FIG. 1 (color online). (a) Surface topography and (b) PFM amplitude image of the $BiFeO_3$ surface before the SS-PFM experiment. (c) SS-PFM work of switching image. (d) Hysteresis loop shape in selected locations in (a). Hysteresis loop fine structure of (e) loop I, (f) loop II and (g) loop III. Shown are corresponding Gaussian fits. The positions and areas for each peak are given in parenthesis. The red circle illustrates the fine-structure feature on the forward branch studied in this work. Vertical scale in (a) is 20 nm.

$$\Phi(r, l) \cong \psi_S S(r, l) - \frac{P_S}{2} \int_V dv (E_3^p(\mathbf{x}) + E_3^d(\mathbf{x})) + \frac{4\pi l r^2}{3\varepsilon_0 \varepsilon_{11}} n_D(r, l) P_S^2, \tag{1}$$

where r is the domain radius, l is its length, S the surface area, ψ_S the domain wall energy density, and P_S the magnitude of spontaneous polarization. The expression for the depolarization factor $n_D(r, l)$ is given in Ref. [20]. The electric field established by the probe is $E_3^p(\mathbf{x}) = -\nabla \varphi_p(\mathbf{x})$, and the electric field created by the defects is $E_3^d(\mathbf{x}) = -\nabla \varphi_d(\mathbf{x})$ (random bond disorder).

Following Ref. [21], we analyze the switching in the presence of a surface field defect. This model is chosen since (a) the PFM probe electric field is maximal on the surface, and hence surface defects affect nucleation more strongly, and (b) the defect concentration near the surface is typically much larger than in the bulk. To develop the analytical description, we adopt the Gaussian field distribution for the ith defect, i.e., assume

$$E_3^d(\mathbf{x}) = E_{Si} \exp\left(- \frac{(x - x_{0i})^2 + (y - y_{0i})^2}{r_{di}^2} - \frac{z}{h_{di}} \right), \tag{2}$$

where E_{Si} is the built-in field amplitude, $h_{di} \ll r_{di}$ is the penetration depth, r_{di} is the characteristic radius, and $\mathbf{x}_{0i} = \{x_{0i}, y_{0i}, 0\}$ is the defect position. The analysis is performed assuming that the semiellipsoidal domain is axisymmetric, but allowing for defect-induced shift of the domain center $\mathbf{b} = \{b_1, b_2, 0\}$ compared to the PFM tip apex location, $\mathbf{a} = \{a_1, a_2, 0\}$ [see Fig. 3(a)]. Thus, $|\mathbf{a} - \mathbf{b}|$ is the tip-domain separation. The domain sizes r, l and position $\mathbf{b}$ are determined from the minimum of free energy in Eq. (1) [22,23].

The schematics of domain evolution for different tip-defect distances are summarized in Fig. 2. The numerical analysis of the switching process illustrates that under conditions $l \gg d$, $l \gg h_{di}$ and $r < d$ (where d is the charge-surface separation or tip size) for large field strength $E_S \cong 10^8$–10^{10} V/m the nucleation process is initiated at the defect location. On increasing the bias, the domain rapidly shifts towards the tip location. The coercive bias shift, $\Delta U_C = U_C^+ + U_C^-$, is

$$\Delta U_C(a_1, a_2) \approx -2 h_{di} E_{Si} \exp\left(- \frac{(x_{0i} - a_1)^2 + (y_{0i} - a_2)^2}{r_{di}^2} \right). \tag{3}$$

This shift is only weakly dependent on the spatial extent of the defect and is determined by the local built-in potential. Hence, the local nucleation biases are a linear superposition of the tip and defect, $h_{di} E_{Si}$, potentials [16].

The immediate consequence of the finiteness of the defect size, $r_{di} < d$, is the emergence of the loop fine structure, as illustrated in Fig. 2. Specifically, for a tip located at the defect site, the switching of the material within the defect occurs for smaller voltages compared to

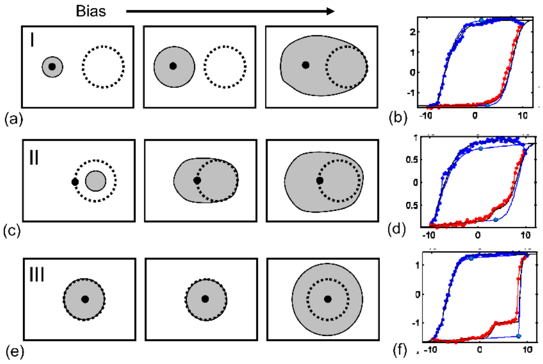

FIG. 2 (color online). Domain growth in the presence of the defect. (a) For large separations, the defect affects domain growth only on late stages and hence does not contribute to the measured signal, corresponding to (b) nearly ideal PFS loops. (c),(d) For intermediate separations, nucleation can be initiated at the defect (rather than tip) site, resulting in a small change in PFM signal for low biases. The domain rapidly shifts towards the tip at higher voltages, resulting in fine structure in PFS. (e) For the tip positioned at the center of the defect, the nucleation starts at low voltages. The growth stops when the domain occupies the defect region, and resumes only when the bias becomes large enough to induce domain growth on the ideal surface. The size of the fine feature (f) is a direct measure of the defect size.

the ideal surface and stops once the domain fills the defect region. The switching of the remaining part of the sample occurs at the same voltages as for an ideal surface. This nonmonotonic growth process results in the fine structure in hysteresis loop, the size of which is determined by the ratio of the signal generation volume of PFM and defect size. Similar behavior is anticipated when the tip is shifted compared to the defect center. However, in this case, nucleation is delayed according to Eq. (3). Finally, for large tip-defect separations the defect volume does not contribute to the observed PFM signal.

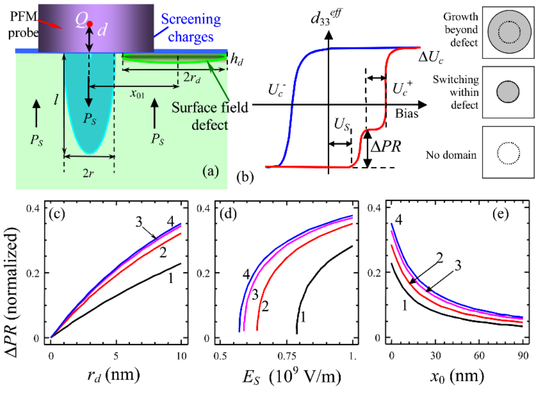

FIG. 3 (color online). (a) Schematics of domain nucleation in the vicinity of surface field defect. (b) Schematic dependence of normalized PR-response on the applied voltage U in the vicinity of defect. The role of single Gaussian defect parameters $\{E_S, h_d, r_d, x_0\}$ on piezoresponse loop fine-structure maximal height ΔPR: (c) $E_S = 0.9 \times 10^9$ V/m, $h_d = 0.4$, 1, 2, 3 nm (curves 1, 2, 3, 4); (d) $r_d = 10$ nm, $h_d = 0.4$, 1, 2, 3 nm (curves 1, 2, 3, 4); (e) $E_S = 0.9 \times 10^9$ V/m, $r_d = 10$ nm, $h_d = 0.4$, 0.6, 1.2, 3 nm (curves 1, 2, 3, 4). Material parameters correspond to BiFeO$_3$ (Ref. [22]), $d = 30$ nm.

Under the condition $\mathbf{b} = \mathbf{x}_{0i}$, the relative change of the piezoelectric response caused by the nearest ith defect is

$$\Delta PR(r_{Si}) \approx \frac{16 r_{Si}}{3d_{33}^* + d_{15}}\left(\frac{3d_{33}^*}{\pi d + 8(r_{Si} + |\mathbf{a} - \mathbf{x}_{0i}|)} + \frac{d_{15}}{3\pi d + 8(r_{Si} + |\mathbf{a} - \mathbf{x}_{0i}|)}\right). \tag{4}$$

The radius of the surface domain state is $r_{Si} = r_{di}\sqrt{\ln(\frac{2h_{di}P_S E_{Si}}{\psi_S + (4h_{di}P_S^2/3\varepsilon_0\varepsilon_{33})})}$, the piezoelectric coefficient is $d_{33}^* = d_{33} + \frac{d_{31}}{3}(1 + 4\nu)$, and ν is the Poisson ratio. Since $r_{Si} \sim r_{di}$, the fine-structure height is a direct measure of the lateral size of the defect.

To verify the theoretical predictions, the spatial variability of hysteresis loop fine structure for the region in Fig. 1 is analyzed. The hysteresis loops have been fitted by a phenomenological fitting function representing the sum of the ideal loop and fine-structure features for forward and reverse branches [Fig. 4(a)] [22]. The nucleation bias map is illustrated in Fig. 4(b). The distribution of the feature strength (total area below the fine-structure feature) is illustrated in Figs. 4(c) and 4(d) for forward and reverse branches. Note that Figs. 4(b) and 4(c) illustrate the expected spatial signature of a single defect—the depression in the nucleation bias image and a ring encircling the defect in the fine-structure image. Further confirmation of this signature is illustrated in averaged radial profiles in Figs. 4(e) and 4(f). The feature is present only on the forward branch of the loop, in agreement with the random-field character of the defect. Therefore, the spectroscopic maps in Figs. 4(b) and 4(c) provide an image of a

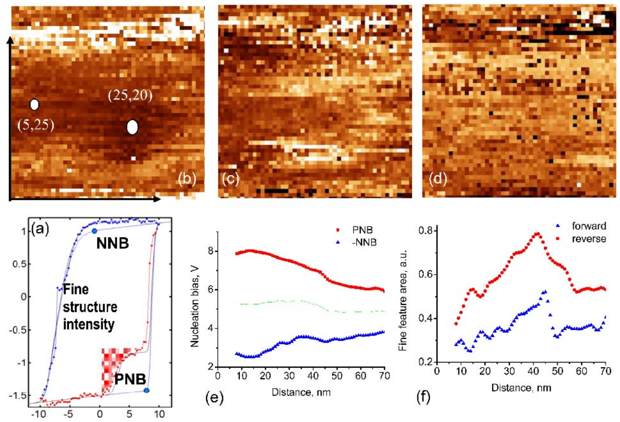

FIG. 4 (color online). (a) Schematics of the hysteresis loop with a single fine-structure feature. 2D maps of (b) negative nucleation bias and integral fine structure for (c) forward and (d) reverse branch. Note the depression in (d) and associated ring structure in (c). Radial averages for (e) nucleation biases and (f) integral fine structure taken with respect to center of defect.

single random-field defect visualized both through the changes in the local nucleation bias, and evolution of the fine-structure feature in the PFS spectra.

Finally, we discuss the relationship between the defect parameters extracted from the image and the single-point spectrum analysis. The characteristic size of the single defect as seen on the PNB image Fig. 4(c) is ~60 nm and built-in potential is ~ -2 V. For these values, the expected magnitude of the fine-structure feature is ~25%–50%, consistent with experimental loop shown in Fig. 4(a). In comparison, the analysis of a single-point hysteresis loop fine structure allows us to estimate $h_d E_S = -3.2$ V, $r_d = 60$ nm for a defect located in cell (25,20). Furthermore, the deconvolution suggests the presence of a second defect with $h_d E_S \approx +0.5$ V, $r_d \approx 30$ nm located in cell (5,25), as can be observed in the spatially resolved image [Fig. 4(b)]. Thus, the defect parameters in the single-point spectra and images are similar, indicative of the self-consistency of the experimental data and fidelity of the theoretical model. Note that real-space data provide better insight into defect location, while spectroscopic data offer significantly higher resolution in energy space.

To summarize, we have predicted the signature of a single defect as the fine structure of hysteresis loops in PFS. Under optimal conditions of tip and surface stability, the measurements are shown to be highly reproducible and hysteresis loops with multiple (up to four) discernible features are demonstrated. The use of a model system with a low density of defects allowed the visualization of a single positive random-field type defect both in the nucleation bias and fine-structure intensity images. Remarkably, the very rich fine structure of the reverse branch of hysteresis loops in Figs. 1(e)–1(g) suggests the presence of multiple negative field defects that cannot be resolved on spatial maps and necessitate the further development of 3D deconvolution algorithms for the SS-PFM data. This will allow the collective effect of defects on switching dynamics to be visualized and probed in real space. These studies of *single- or several defect* effects on domain nucleation and wall motion complement the macroscopic and mesoscopic imaging studies [12] that allow *collective* effect of defects on wall dynamics to be probed.

From a general perspective, scanning probe microscopy (SPM) provides a natural platform for local studies of phase transitions and chemical reactions. The best known example is protein unfolding spectroscopy, in which a force applied by an SPM tip to an individual macromolecule acts as a stimulus for conformational changes and the length provides readout of the molecular state [24]. However, this example is unique—in cases such as pressure induced phase transitions (e.g., dislocation nucleation during indentation process) the process is irreversible, precluding systematic studies of the role of defects. The spectroscopic imaging approach can be combined with other detection methods, e.g., Raman, optical, or electroluminescent detection, to study a broad range of reversible bias-induced phenomena, including crystallization amorphization in phase change memories or electrochemical reactions. This will open the pathway for studies of defect-engineered systems and hence understanding of atomistic mechanisms of these transformations.

Research was sponsored in part (S. J., B. J. R.) by the Division of Materials Sciences and Engineering, and in part (S. V. K.) by the Center for Nanophase Materials Sciences, Office of Basic Energy Sciences, U.S. Department of Energy, and (Y. H. C., R. R.) by the Division of Materials Sciences and Engineering under Contract No. DE-AC02-05CH11231.

---

*Corresponding author.
sergei2@ornl.gov

[1] J. Scott, *Ferroelectric Memories* (Springer-Verlag, Berlin, 2000).
[2] T. Tybell, C. H. Ahn, and J.-M. Triscone, Appl. Phys. Lett. **72**, 1454 (1998).
[3] S. P. Alpay *et al.*, Appl. Phys. Lett. **85**, 2044 (2004).
[4] I. I. Naumov, L. Bellaiche, and H. Fu, Nature (London) **432**, 737 (2004).
[5] S. K. Streiffer *et al.*, Phys. Rev. Lett. **89**, 067601 (2002).
[6] C. L. Jia *et al.*, Nat. Mater. **7**, 57 (2008).
[7] R. Landauer, J. Appl. Phys. **28**, 227 (1957).
[8] J. F. Scott, J. Phys. Condens. Matter **18**, R361 (2006).
[9] A. Gruverman *et al.*, Appl. Phys. Lett. **87**, 082902 (2005).
[10] D. J. Kim *et al.*, Appl. Phys. Lett. **91**, 132903 (2007).
[11] A. Grigoriev *et al.*, Phys. Rev. Lett. **96**, 187601 (2006).
[12] T. Tybell *et al.*, Phys. Rev. Lett. **89**, 097601 (2002).
[13] T. Natterman, Y. Shapir, and I. Vilfan, Phys. Rev. B **42**, 8577 (1990).
[14] V. Repain *et al.*, Europhys. Lett. **68**, 460 (2004).
[15] S. V. Kalinin *et al.*, Proc. Natl. Acad. Sci. U.S.A. **104**, 20 204 (2007).
[16] S. Jesse *et al.*, Nat. Mater. **7**, 209 (2008).
[17] Y. H. Chu *et al.*, Appl. Phys. Lett. **90**, 252906 (2007).
[18] S. Jesse, H. N. Lee, and S. V. Kalinin, Rev. Sci. Instrum. **77**, 073702 (2006).
[19] M. Molotskii, J. Appl. Phys. **93**, 6234 (2003).
[20] E. M. Lifshitz, L. D. Landau, and L. P. Pitaevskii, *Electrodynamics of Continuous Media* (Butterworth-Heinemann, London, 1984).
[21] G. Gerra, A. K. Tagantsev, and N. Setter, Phys. Rev. Lett. **94**, 107602 (2005).
[22] A. N. Morozovska *et al.*, (to be published); arXiv:0711.1426.
[23] See EPAPS Document No. E-PRLTAO-100-052815 for supplementary information for the manuscript. For more information on EPAPS, see http://www.aip.org/pubservs/epaps.html.
[24] M. Rief *et al.*, Science **275**, 1295 (1997).